Oxygen Nonstoichiometry in $(Ca_2CoO_3)_{0.62}(CoO_2)$: A Combined Experimental and Computational Study

*Matthias Schrade[1], Simone Casolo[2], Paul J. Graham[3], Clemens Ulrich[3], Sean Li[4], Ole-Martin Løvvik[1,5], Terje G. Finstad[1], and Truls Norby[6,]**

[1] Centre for Materials Science and Nanotechnology, Department of Physics, University of Oslo, FERMiO, Gaustadalléen 21, NO-0349 Oslo, Norway

[2] Dipartimento di Chimica, Università degli Studi di Milano, via Golgi 19, 20133 Milan, Italy

[3] School of Physics, The University of New South Wales, Sydney, NSW 2052, Australia

[4] School of Materials Science and Engineering, The University of New South Wales, Sydney NSW, 2052, Australia

[5] SINTEF Materials and Chemistry, Forskningsveien 1, NO-0314 Oslo, Norway

[6] Centre for Materials Science and Nanotechnology, Department of Chemistry, University of Oslo, FERMiO, Gaustadalléen 21, NO-0349 Oslo, Norway

Corresponding Author

*E-mail: t.e.norby@kjemi.uio.no, Tel: +47-22840654, Centre for Materials Science and Nanotechnology, Department of Chemistry, University of Oslo, FERMiO, Gaustadalléen 21, NO-0349 Oslo, Norway

Abstract

The oxygen nonstoichiometry in the misfit calcium cobaltite $(Ca_2CoO_3)_{0.62}(CoO_2)$ has been studied experimentally and by density functional theory (DFT) calculations. The standard oxidation enthalpy ΔH^0_{Ox} of oxygen deficient $(Ca_2CoO_3)_{0.62}(CoO_2)$ was measured directly using simultaneous thermogravimetry and differential scanning calorimetry (TG-DSC). ΔH^0_{Ox} was found to be in agreement with the prediction from a previously published defect chemical model based on purely thermogravimetrical analysis. A series of samples with different oxygen vacancy concentration was prepared by annealing in air, followed by rapid quenching. Room temperature Raman spectroscopy showed a sharp mode at 700 cm^{-1} decreasing in intensity with increasing vacancy concentration. We discuss this observation as evidence for oxygen vacancies being preferably formed within the central layer of the Ca_2CoO_3 subsystem. DFT calculations demonstrated that the calculated electronic structure is sensitive to the chosen model of the crystal structure. Still, for all investigated models, the standard formation enthalpy of oxygen vacancies within the Ca_2CoO_3-moiety was much lower than that for a site within the CoO_2-layer, in agreement with the presented experimental data.

Keywords: Thermoelectric Oxides, misfit calcium cobaltite, $(Ca_2CoO_3)_{0.62}(CoO_2)$, $Ca_3Co_4O_9$, Oxygen nonstoichiometry

1. Introduction

The family of misfit cobaltites has attracted significant scientific interest in recent years due to their interesting electronic properties, the intriguing crystal structure, and the interplay between the two.[1] The common building block of misfit cobaltite structures is a layer of edge sharing CoO_6 octahedra (hereafter denoted as the cobalt oxide layer, COL), which is alternately stacked along the *c* axis with layers of rock salt symmetry (rock salt layer, RSL), thereby forming a natural superlattice along the *c* axis.[2] Interesting electronic properties of these materials result from charge transfer between the two subsystems, leading to a mixed valent cobalt state within the COL.[3]

In this paper, we study the misfit calcium cobalt oxide (CCO), where the COL is separated by Ca_2CoO_3 as the rock salt subsystem. While the *a*- and *c*-axes of both the COL and RSL subsystem are identical, the *b*-axes are not, and the ratio of b_{COL} and b_{RSL} leads to a structural modulation along *b*. The most precise notation for CCO is thus $(Ca_2CoO_3)_q(CoO_2)$ with $q = b_{COL}/b_{RSL} = 0.62\pm0.03$,[4-6] but the alternative notation "$Ca_3Co_4O_9$" is frequently found in the literature as well. CCO doped with various elements has been intensively studied as a thermoelectric material suitable for high temperature energy harvesting and exhibits one of the highest figure of merit among all oxide materials (e.g. [7]).

At high temperatures, the electronic properties of many oxide materials are influenced by reduction: thermal creation of effectively positively charge oxygen vacancies and the accompanying change in the concentration of electronic charge carriers. Using the Kröger-Vink

notation,[8] the formation of an oxygen vacancy, charge compensated by two hole type carriers, can be written as:

$$O_O^x + 2h^\bullet = v_O^{\bullet\bullet} + \tfrac{1}{2}O_2 . \quad (1)$$

While there has been some discussion about the presence and degree of oxygen nonstoichiometry in the structurally related compound Na_xCoO_2,[9-12] it is generally agreed that CCO can exhibit a significant amount of oxygen vacancies: Previous studies have shown the reversible creation of oxygen vacancies in CCO at high temperatures and atmospheres with a low oxygen partial pressure pO_2 (e.g. [4, 13-14]). Writing the chemical formula as $Ca_3Co_{3.92}O_{9.34-\delta}$, Shimoyama *et al.* showed that CCO can accommodate oxygen vacancies up to $\delta = 0.20$ without decomposition.[13] Based on an X-ray diffraction refinement study, Ling *et al.* concluded that oxygen vacancies are exclusively formed in the central Co-O layer of the RSL-subsystem.[6] Oxygen vacancies inside the RSL may adjust the charge carrier concentration, without disturbing the conduction path of carriers inside the COL by acting as scattering centers.

The presence of oxygen vacancies could therefore be a possible reason for reported discrepancies in the electronic properties of nominally identical samples (e.g. [7]). Further, oxygen vacancies may also affect the internal stress between the two subsystems, thereby causing the different structural modulations observed experimentally.[15-16]

The oxidation/reduction thermodynamic behavior of a material is usually studied by means of thermogravimetry or coulometric titration (e.g. [17-18]), and the extraction of equilibrium coefficients and standard entropies and enthalpies relies on the validity of several assumptions. These assumptions include the negligible temperature dependence of the thermodynamic parameters and not least the applicability of the considered defect chemical model. It is therefore desired to employ a technique allowing the direct determination of parameters for the

thermodynamic reduction (or oxidation) processes. This is done here by an instrument, combining thermogravimetry and differential scanning calorimetry (TG-DSC), where the enthalpy change is measured directly and simultaneously with the respective mass change upon sample reduction or oxidation. When the chemical reaction involved is identified, the enthalpy change of the reaction is readily obtained from the TG-DSC analysis.

The incommensurate structure of misfit compounds makes it difficult to describe them computationally, as relatively big unit cell approximations and high computational power are required. Previous attempts to model the electronic structure of CCO have led to results contradicting experimental evidence or have shown to be sensitive towards the chosen unit cell.[19-20]

Recently, we have presented a defect chemical model to describe the oxygen nonstoichiometry in CCO, which is based on the assumption that oxygen vacancies are only formed next to Co^{2+} sites within the central Co-O-layer in the rock salt subsystem.[21]

In this paper, we report on our results of a combined experimental and computational study of oxygen nonstoichiometry in CCO. Density functional theory (DFT) calculations and Raman spectroscopy give further evidence that oxygen vacancies are mainly formed in the central Co-O layer of the rock salt subsystem. The oxidation thermodynamics in CCO are studied directly by TG-DSC, and the results are compared to values obtained from DFT and the defect chemical modeling.

2. Experimental Methods

Powder and pellet samples of CCO with a Ca to Co ratio of 3 to 3.95 were fabricated as reported elsewhere.[21] The change in oxygen content of a pellet was determined by means of thermogravimetry (CI Electronics MK2 microbalance). The sample and the counterweight were

attached to the arms of the balance using platinum wires. The sample was hanging in an outer alumina tube in a vertical tubular furnace and the counterweight was hanging in a glass tube kept at room temperature. The apparatus was connected to an in-house built gas mixer of a type as described elsewhere.[22] The weight change was monitored when varying the oxygen partial pressure (pO_2) from 1 to 10^{-4} atm by diluting O_2 with He until equilibrium was obtained. All measurements were performed for temperatures and pO_2 where CCO is stable.[13] The observed weight change can thus be solely assigned to a variation of the oxygen stoichiometry. In practice, a resolution of ~ 0.01 mg was obtained, which translates to a resolution in the oxygen nonstoichiometry δ in $Ca_3Co_{3.92}O_{9.34-\delta}$ of ~ 0.0003 for our sample masses. All weights were corrected for estimated buoyancy arising from the asymmetrical temperature and volume of the sample and counterweight.

To study the oxidation thermodynamics of oxygen deficient CCO, we use an instrument with simultaneous thermogravimetry and differential scanning calorimetry (TG-DSC) (Netzsch STA 449 C Jupiter), connected to a similar gas mixer as for the pure thermogravimetric measurements. The DSC signal is a measure of the heat flow from the sample in comparison to an empty reference crucible. When the sample undergoes a reaction associated with an enthalpy change (e.g. a phase transition or chemical decomposition), the DSC curve shows a peak, where the peak area corresponds to the respective change in enthalpy.

Since CCO is stable at the temperatures and pO_2 used in the TG-DSC experiments, the observed signals can be associated with the formation/oxidation of oxygen vacancies. The DSC-peak area, divided by the corresponding mass change, can thus be identified with the oxidation enthalpy ΔH_{Ox} of oxygen deficient CCO.

Instrument and crucible calibration was done right before the measurement of the sample, by using reference samples with structural phase transitions in the investigated temperature range. As for the TG experiment, the pO_2 was varied by diluting O_2 in He. At each temperature, three oxidation and reduction cycles were recorded to increase the statistical significance and only the exothermic oxidation signal was used for peak integration.

Ceramic samples of CCO were prepared with different oxygen nonstoichiometries for Raman spectroscopy measurements. These samples were obtained by annealing in air at different temperatures well below the decomposition temperature of CCO until compositional equilibrium was reached and then rapidly (≈ 15 s) cooled to room temperature. The surface was polished after quenching.

Room temperature Raman measurements were performed with a Dilor XY triple grating Raman spectrometer in back-scattering configuration using the unpolarized 514.5 nm laser line of a Coherent Innova 90 Ar^+/Kr^+ mixed-gas laser. The samples measured were placed with the compacting direction (mainly the *c* axis) parallel to the incident laser beam. In order to avoid heating of the sample, the power of the laser was kept below 20 mW, and was focused onto the surface of the samples with a spot size of ≈ 100 nm in diameter.

3. Theoretical and Computational Methods

We adopted a computational methodology similar to that successfully used before by Rébola *et al.*:[19] Spin polarized periodic DFT calculations were performed using the VASP package.[23] The plane wave basis set was limited to a 600 eV energy cut-off for valence electrons while the atomic cores were included via the projector augmented wave (PAW) method.[24] The Brillouin zone was sampled by a Γ-centered grid of 3×2×3 *k* points (placed less than 0.035 $2\pi/|a|$ from each other in reciprocal lattice direction). The exchange and correlation effects were embodied

by the Perdew–Burke–Ernzerhof (PBE) generalized gradient functional.[25] Simultaneous relaxation of ionic positions and lattice parameters was performed for the defect free monoclinic structures starting from the experimental values a = 4.83 Å, c = 10.84 Å, β = 98.1° along the periodic directions. Along the incommensurate direction we used multiples of the COL parameter b = 2.82 Å.[16] The optimized cell vectors were kept fixed when computing the equilibrium structure for the defective phases. Ionic positions were relaxed until the maximum force acting on each ion was lower than 0.05 eV/Å.

The considered CCO unit cells were built by rational approximants, i.e. by using multiples of CoO_2 and Ca_2CoO_3 units that are consecutive numbers of the Fibonacci sequence F(n), namely as $(Ca_2CoO_3)_{F(n)}(CoO_2)_{F(n+1)}$, hence following a misfit ratio q=F(n)/F(n+1) = 2/3, 3/5, 5/8, 8/13, … [12]. This simple relationship arises from the fact that the ratio of two subsequent numbers of the Fibonacci sequence converges to the golden ratio (F(n)/F(n+1)=0.618, n→∞) which is remarkably similar to the experimental misfit q = 0.620±0.003.[2, 4, 16] We restricted our calculations to the 2/3 and 3/5 rational approximations, but expanded the simulated cell along the shortest lattice vector a to minimize interactions between periodic images of the charged defects. In order to have a similar cell volume – and thus comparable vacancy concentrations when calculating on the defective cell – we used a 3×1×1 and a 2×1×1 supercell for the 2/3 and 3/5 model, respectively. The main difference between the two models thus lies in the misfit ratio. The unit cell described by the rational approximation 2/3 corresponds to a chemical formula $(Ca_2CoO_3)_{12}(CoO_2)_{18}$ (q = 0.67) while the 3/5 cell corresponds to $(Ca_2CoO_3)_{12}(CoO_2)_{20}$ (q = 0.60).

To treat the formation of oxygen vacancies – reaction 1 in reverse direction - in a computational framework, we considered the following chemical reaction (written for the 3/5 unit cell and without assuming a certain oxygen position for the formation of oxygen vacancies):

$$\mathrm{Ca_{24}Co_{32}O_{76}} = \mathrm{Ca_{24}Co_{32}O_{75}} + \tfrac{1}{2}\mathrm{O_2} + \mathrm{v_O^{\bullet\bullet}} + 2e' . \quad (2)$$

We computed the standard formation enthalpy $\Delta H_{\mathrm{form}}(p^0,T{=}0)$ for oxygen vacancies from this by

$$\Delta H_{\mathrm{form}}(p^0,0) = H_{\mathrm{def}}(p^0,0) - H_{\mathrm{perf}}(p^0,0) + \frac{1}{2}\cdot H_{\mathrm{O_2}}(p^0,0) + 2\mu_e \ , \quad (3)$$

where $H_{\mathrm{perf}}(p^0,0)$ and $H_{\mathrm{def}}(p^0,0)$ are the enthalpies for the pristine and defective structures, respectively, and $\Delta H_{\mathrm{O2}}(p^0,0)$ is that of oxygen gas. All enthalpies are taken at standard pressure p^0 = 1 bar and temperature T = 0 K, and assumed to correspond to the DFT total energies. The system charge n (here n = 2 for an oxygen vacancy with a double positive effective charge) was simulated by adjusting the total number of electrons in the cell and at the same time adding a compensating jellium background to avoid diverging Coulomb contributions. The electron potential μ_{e} was defined as

$$\mu_{\mathrm{e}} = E_{\mathrm{F}} + \gamma = E_{\mathrm{F}} + \left(V_{\mathrm{def}} - V_{\mathrm{perf}}\right), \quad (4)$$

where E_{F} is the Fermi level in the pristine material. γ is a correction term which accounts for the energy of the jellium-like potential, here considered as the shift in the average electrostatic potentials at a bulk-like lattice site far from the vacancy in the defective (V_{def}) and pristine (V_{perf}) supercell.[26-27]

Eq. 3 could be extended to obtain ΔG_{form} at finite temperatures and oxygen partial pressures.[10, 28] However, as this is usually based on several assumptions (e.g. that thermal contributions of the solid are negligible compared to that of the gas; $G_{\mathrm{i}}(p,T) = G_{\mathrm{i}}(p^0,0)$), the association between

experiment and calculation will in this work be done at 0 K by comparing the computational formation enthalpy of an oxygen vacancy to the experimental results.

4. Results and discussion

4.1. Thermogravimetry and Defect Chemical Model

The measured oxygen nonstoichiometry δ in $Ca_3Co_{3.92}O_{9.34-\delta}$ as a function of pO_2 and temperature T is shown in Fig. 1. The data is identical to those published in [21] but plotted as $Ca_3Co_{3.92}O_{9.34-\delta}$ instead of $(Ca_2CoO_{3-\Delta})_{0.62}(CoO_2)$ (with $\Delta = 0.62 \times \delta$) in order to not presuppose a certain site for oxygen vacancy formation. We use the weight at 350°C and pO_2 = 1 atm as a reference for $\delta = 0$.

The defect chemical model to describe oxygen nonstoichiometry and other relevant electronic defects in CCO is explained in detail elsewhere,[21] but we present the main features here.

Due to the incommensurate stacking of the Ca_2CoO_3 and the CoO_2 layers, a mixed-valent state for the Co-ions within the COL is inherently present. As a perfect reference state, we define that all Co-atoms in the rock salt layer are in a 3+ state, which results in a mixed valent state with an average valency of 4-q = 3.38 in the CoO_2 layer, in order to satisfy overall charge neutrality.

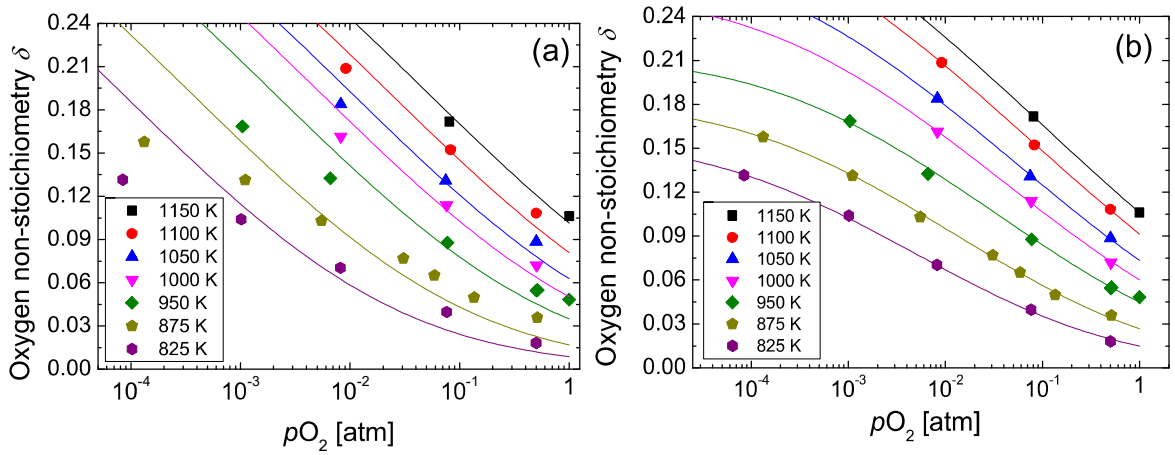

Figure 1. Oxygen nonstoichiometry δ in CCO vs. oxygen partial pressure pO_2 at different temperatures. (a) A numerical fit using Eq. 6, 8, and 9 does not describe the experimental data properly. (b) The fit quality improves significantly by including an additional site restriction as explained in the text.

When choosing a localized representation, an electron charge carrier can be identified with a Co^{3+}-ion, and thus carries an effective charge of –(1-q), while a hole carrier (or Co^{4+}-ion) has an effective charge of +q. In the following, we use a modified Kröger-Vink-notation [29] and subscripts RSL or COL to denote the specific location of each defect.

In this notation, the oxidation of an oxygen vacancy (Eq. 1) can be written as

$$\mathrm{v}_{\mathrm{O}}^{\bullet\bullet} + \tfrac{1}{2}\mathrm{O}_2(\mathrm{g}) + 2\mathrm{e}_{\mathrm{COL}}^{(1-q)/} = \mathrm{O}_{\mathrm{O}}^{\mathrm{x}} + 2\mathrm{h}_{\mathrm{COL}}^{q\bullet}, \tag{5}$$

with the equilibrium coefficient

$$K_{\mathrm{Ox}} = \frac{\left[\mathrm{O}_{\mathrm{O}}^{x}\right]\cdot\left[\mathrm{h}_{\mathrm{COL}}^{q\bullet}\right]^2}{\left[\mathrm{v}_{\mathrm{O}}^{\bullet\bullet}\right]\cdot\left[\mathrm{e}_{\mathrm{COL}}^{(1-q)/}\right]^2\cdot\sqrt{p\mathrm{O}_2}} = \exp\left(-\frac{\Delta G_{\mathrm{Ox}}}{\mathrm{k_B}T}\right) = \exp\left(-\frac{\Delta H_{\mathrm{Ox}}}{\mathrm{k_B}T}\right)\cdot\exp\left(\frac{\Delta S_{\mathrm{Ox}}}{\mathrm{k_B}}\right). \tag{6}$$

ΔG_{Ox}, ΔH_{Ox}, and ΔS_{Ox} are the Gibbs energy, the enthalpy, and the entropy of the oxidation reaction, respectively.

Equivalently, one can consider Eq. 5 in the reverse direction. The reaction then describes the formation of an oxygen vacancy – in analogy to the process studied by DFT (Eq. 2). The corresponding thermodynamic parameters for oxygen vacancy formation are then the negative of the respective parameters of the oxidation reaction $\Delta G_{\mathrm{form}} = -\Delta G_{\mathrm{Ox}}$, $\Delta H_{\mathrm{form}} = -\Delta H_{\mathrm{Ox}}$, and $\Delta S_{\mathrm{form}} = -\Delta S_{\mathrm{Ox}}$.

The experimental δ shows signs of saturation at low pO_2, where the saturation level increases with temperature. We therefore suggested a thermal excitation of hole type charge carriers within the COL and a compensating reduction of Co^{3+} to Co^{2+} in the rock salt layer in:[21]

$$Co^{x}_{Co,RSL} + e^{(1-q)/}_{COL} = Co^{/}_{Co,RSL} + h^{q\bullet}_{COL}, \quad (8)$$

$$K_D = \frac{\left[Co^{/}_{Co,RSL}\right] \cdot \left[h^{q\bullet}_{COL}\right]}{\left[Co^{x}_{Co,RSL}\right] \cdot \left[e^{(1-q)/}_{COL}\right]} . \quad (9)$$

Further, the overall electroneutrality requires:

$$q \cdot \left[Co^{/}_{RSL}\right] + (1-q) \cdot \left[e^{(1-q)/}_{COL}\right] = q \cdot \left[h^{q\bullet}_{COL}\right] + 2 \cdot q \cdot \left[v^{\bullet\bullet}_{O}\right] . \quad (10)$$

A numerical fit of the thermogravimetric data to these equations describes the experimental results only qualitatively (e.g. R^2 = 0.84 at 675°C) (Fig. 1 (a)). We therefore included an additional, plausible restriction in:[21] We postulated that oxygen vacancies can only be formed on oxygen sites next to Co^{2+} ions in the rock salt layer, rationalized by a weaker chemical bond between those two species as compared to a Co^{3+}-site. The resulting model allows fitting the thermogravimetric data to the equilibrium constants of the two equations and describes the data very well (R^2=0.997 at 675°C) (Fig. 1 (b)). The obtained thermodynamic parameters for charge disproportionation (Eq. 9) and oxidation (Eq. 6) follow an Arrhenius-type behavior with the oxidation enthalpy ΔH_{Ox} determined to -53 ± 2 kJ/mol (equivalent to a formation enthalpy of ΔH_{form} = 0.57 ± 0.02 eV per oxygen vacancy).

4.2. Raman Spectroscopy

Room temperature Raman spectra of ceramic CCO samples with different oxygen content are shown in Fig. 2. The phonon modes found in the investigated spectral range from 250 – 800 cm^{-1} can be ascribed to vibrational motion of oxygen, rather than the heavier Ca and Co atoms.[30] The δ values for the respective samples were estimated from Fig. 1 (b). The spectra were normalized to the intensity of the mode at 630 cm^{-1}. We note, however, that a normalization over the whole spectral range yields qualitatively similar results. Each spectrum is dominated by three modes at

300, 540, and 630 cm^{-1}. In addition, the spectrum is built up of a range of broad, overlapping modes, which are in general agreement with a Raman study of CCO single crystals.[30] The assignment of these modes is challenging due to the complicated structure of CCO and beyond the scope of this paper. By comparing our results to the reported Raman spectrum of Na_xCoO_2 - which has a similar layer of edge-sharing CoO_6 octahedra – we note that the latter is dominated by modes at 475 and 570 cm^{-1} at room temperature, which have been assigned, respectively, to the in-plane E_{1g} and out-of-plane A_{1g} modes.[31-32] In analogy, we therefore assign the dominant modes found in CCO at 540 and 630 cm^{-1} to the E_{1g} and A_{1g} mode, respectively. The energy shift as compared to NCO is caused by slightly different lattice parameters and different interlayer strain between the two subsystems.

When creating oxygen vacancies in the structure, the most prominent change in the Raman spectra of Fig. 2 is the suppression of the sharp mode at 700 cm^{-1} with increasing δ. Further, the intensity of the mode at 290 cm^{-1} decreases slightly, while the spectral weights of the other modes remain roughly unchanged (see Fig. 2 c). Also, the positions of the peaks shift slightly to higher wavenumbers with increasing δ, thereby indicating a variation of the internal stress between the two layers. For example, the peak of the most intense mode shifts gradually from 625 cm^{-1} for $\delta = 0$ to 633 cm^{-1} for $\delta = 0.15$ (Fig. 2 b).

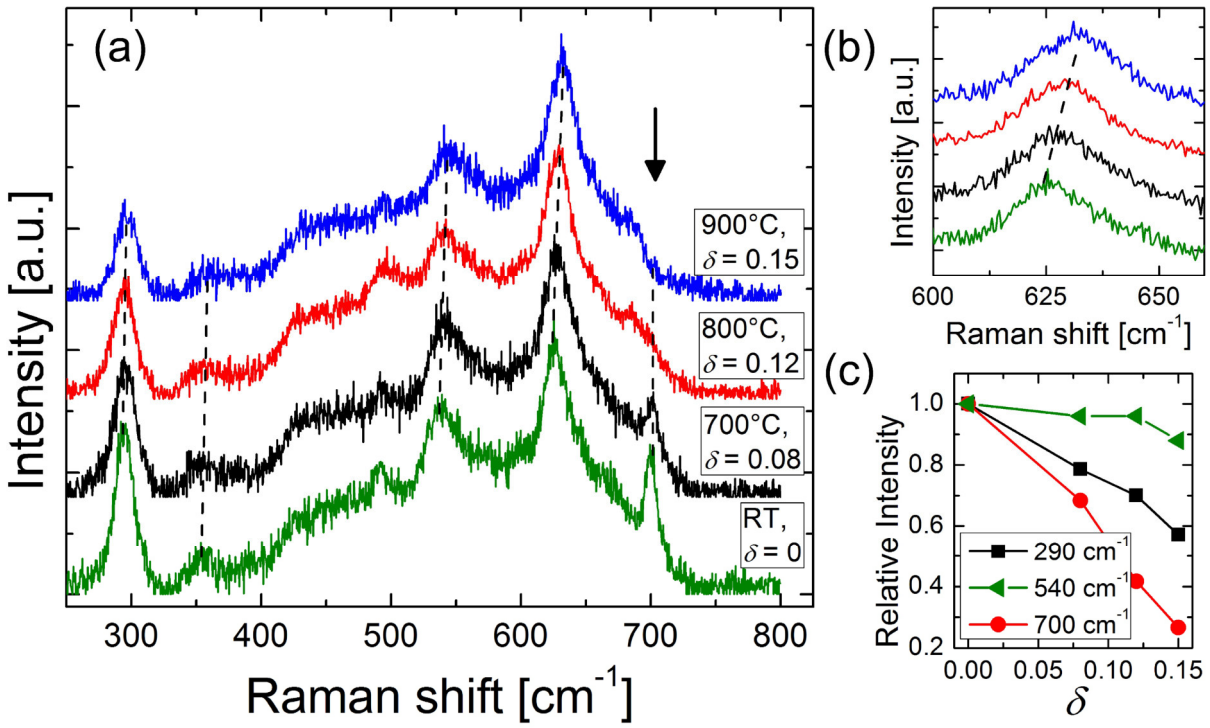

Figure 2. (a) Raman spectra for CCO measured at room temperature. The curves have been offset vertically for clarity. The samples were annealed in air at different temperatures and quenched. The intensity of the mode at 700 cm^{-1} (marked with an arrow) decreases with increasing δ. Dashed lines are a guide to the eye for the peak positions. (b) Detail of the mode at 625 cm^{-1}. The peak position shifts to higher wavenumbers with increasing δ. (c) The relative intensity of three dominant modes as a function of δ.

If we assume a significant formation of oxygen vacancies within the CoO_2 layer, several modes connected to the vibration and rotation of the CoO_6 octahedra would be affected by the removal of oxide ions, both by changing the respective energy as well as the intensity. In particular, such changes should be visible for the E_{1g} and A_{1g} modes, likely at 540 and 630 cm^{-1}. Since only the modes at 290 and 700 cm^{-1} show a significant change upon the formation of

oxygen vacancies, we conclude that no significant oxygen nonstoichiometry is present within the CoO_2 layer.

We therefore assign both modes at 290 and 700cm^{-1} to vibrations within the rock salt layer. A mode similar to the one at 700 cm^{-1} with the same annealing behavior was observed in Co-doped ZnO (at 690 cm^{-1}) with different concentrations of oxygen vacancies and identified as a local disordered vibrational mode of a Zn-O-Co-cluster.[33] In that material, oxygen vacancies are preferentially formed close to Co-dopant sites in Zn-O, so that the mode at 690 cm^{-1} loses its spectral weight when the sample is annealed in an oxygen poor atmosphere and recovers upon annealing in air. In analogy, we therefore assign the mode observed in CCO at 700 cm^{-1} with a local vibration of a Co-O-Co-…-cluster within the rock salt subsystem. By creating oxygen vacancies on those oxygen sites, the spectral weight of the corresponding mode is expected to decrease, as observed experimentally.

For $\delta = 0.15$, the relative spectral weight at 700 cm^{-1} is reduced to ≤ 25 % of its value for $\delta = 0$ (Fig. 2 (c)), indicating that the associated vibrating Co-O-Co-…-cluster extends over several Co-O-units. The formation of oxygen vacancies could induce a structural clustering of the RSL - as discussed in detail in section 4.4 – which impedes the vibration of Co-O-Co-…-clusters associated with the Raman-active mode at 700 cm^{-1}. We emphasize that the mode at 700 cm^{-1} is not a defect mode, but a Raman active mode, present in the perfect structure, and suppressed upon defect formation. In summary, the results obtained from Raman spectroscopy suggest that oxygen vacancies are mainly formed on sites within the central Co-O layer inside the rock salt subsystem.

4.3. Direct Investigation of Oxidation Thermodynamics

The defect chemical model presented in section 4.1. contains a set of assumptions and simplifications. It is thus desired to measure the oxidation enthalpy of CCO in a more direct way, to allow for a critical assessment of the predictions made from this model. Simultaneous thermogravimetry and differential scanning calorimetry (TG-DSC) allows an unambiguous measurement of the enthalpy change connected to the exchange with oxygen.

As an example, the raw data of a TG-DSC oxidation experiment of CCO at 1050 K is shown in Fig. 3. After ten minutes - when both the TG and DSC signals were stable - the oxygen partial pressure pO_2 within the measurement chamber was changed from approximately 0.1 to 1 atm. The sample weight increased and the DSC-signal showed an exothermic peak. Both observations can be assigned to the oxidation of oxygen vacancies in CCO. We note that the exact knowledge of the pO_2 and thus the oxygen vacancy concentration in both states is not required to extract the molar oxidation enthalpy as only the differential $\Delta H/\Delta m$ is needed for the calculation. When both signals were stable again, the atmosphere was changed back to a pO_2 of 0.1 atm. The measurement was repeated twice to increase the statistical significance of the obtained result.

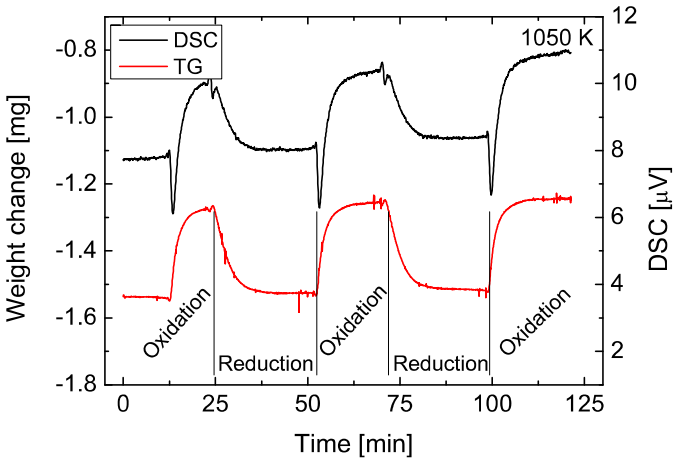

Figure 3. Isothermal TG-DSC raw-data obtained at 1050 K. When switching the pO_2 from 0.1 atm to 1 atm, a sharp, exothermic peak is observed in the DSC signal, accompanied by a weight

increase. The corresponding endothermic peak for the sample reduction is less clear due to the slower reaction kinetics and the slower gas phase exchange in the case of dilution.

The DSC signal in Fig. 3 shows a very different equilibrium value for the two different atmospheric compositions (10% O_2 diluted in He and pure O_2), due to variations in the heat capacity and heat conductivities of the different atmospheres, thereby changing the heat flow from the crucible in both conditions. To allow a meaningful integration of the DSC peak, we therefore recorded a DSC background of an empty crucible under similar experimental conditions. A typical background is shown in Fig. 4 (a). Some experimental limitations have to be considered before background subtraction can be done: The switch in the atmospheric composition cannot be done instantaneously, but several flowmeters of the gas mixer have to be adjusted manually. The onset time of the DSC-signal for both the sample and background shown in Fig. 4 (a) can therefore only be determined with an accuracy of approximately 15 s, as indicated by the two times t_i and t_{i+1}. In practice, this inaccuracy corresponds to a horizontal shift of the background with respect to the DSC signal of the sample when subtracting the background. We subtracted the background for the two extreme conditions of an early and late onset, respectively. The two resulting peaks are shown in Fig. 4 (b). Using a sigmoidal baseline, the area for the two peaks typically differs by 20%, indicating the statistical inaccuracy of the extracted data. The error in $\Delta H/\Delta m$ due to different integration boundaries of both DSC- and TG-signal is in the order of 3% and therefore negligible as compared to that of background subtraction.

The resulting oxidation enthalpies in the investigated temperature range lie between -39 and -68 kJ/mol (corresponding to a formation enthalpy of ΔH_{form}= 0.40 - 0.71 eV per oxygen vacancy for the reverse process) and do not show a clear temperature trend (Fig. 5). The extracted values

are in good agreement with the oxidation enthalpy $\Delta H_{Ox} = -\Delta H_{Red} = -53$ kJ/mol (equivalent to $\Delta H_{form} = 0.55$ eV), derived from the defect chemical model based on a pure thermogravimetric analysis. These results thus provide further evidence for the applicability of the defect chemical model and the validity of the employed assumptions. In particular, the TG-DSC results thereby support the analysis and conclusion we made for the charge transport in CCO.[21]

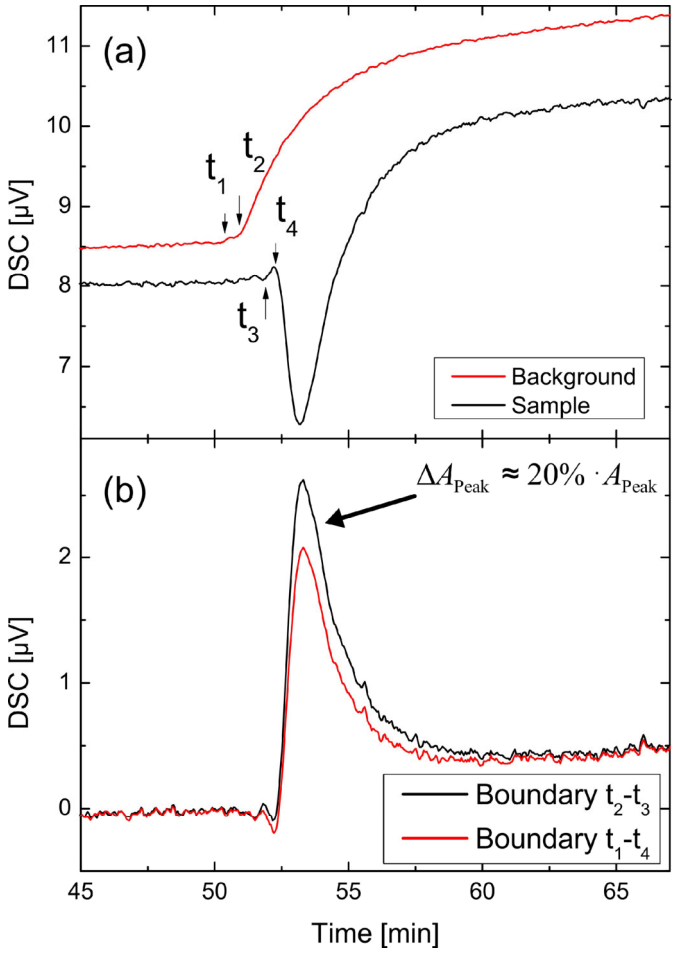

Figure 4. (a) DSC signal of a sample and a blank crucible under oxidation. The background line is vertically shifted for clarity. Different, extreme onset-times are used for background subtraction. (b) Extracted peaks for the two extreme pairs of onset times. The integrated areas of both peaks typically differ by 20%.

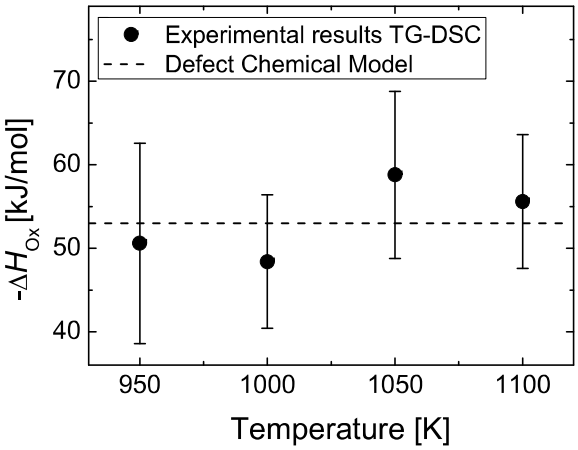

Figure 5. The molar oxidation enthalpy of CCO at different temperatures *T* as obtained by TG-DSC. The extracted values do not show a clear *T* dependency. The value predicted from the defect chemical model is indicated for comparison (dashed line).

4.4. Computational Results

In parallel to the experimental investigations, we addressed the oxygen nonstoichiometry in CCO computationally. In particular, we aimed to check the crystallographic restriction of oxygen vacancies within the RSL, by calculating the formation enthalpies of oxygen vacancies placed at different oxygen sites.

We first studied the geometric structure of pristine CCO for different structural models. Based on these results, we calculated the formation energy of an oxygen vacancy placed in different crystallographic positions. Finally, we compared the obtained electronic properties for the different structures and computational methods.

As mentioned in Section 3, we restricted our calculations to the 3/5 (q = 0.60) and 2/3 (q = 0.67) unit cells to approximate the incommensurately modulated structure of CCO. The relaxed cells for the two structural models we used are shown in Fig. 6.

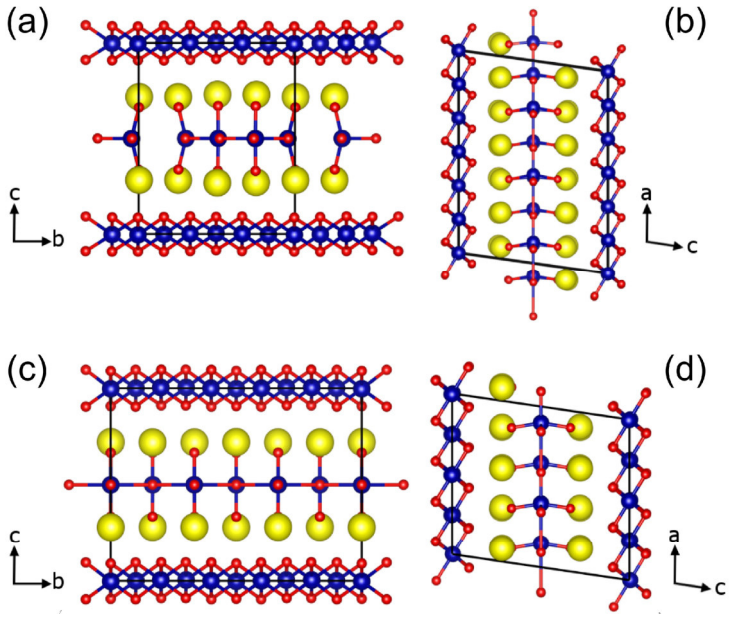

Figure 6. Relaxed unit cells of CCO used in the DFT modeling. Red, blue, and yellow balls represent oxygen, cobalt, and calcium, respectively. (a) and (b): Relaxed 2/3 unit cell seen from different directions. Clustering of the central of Ca_2CoO_3 layer along the b axis is visible. (a=4.89 Å, b_{RSL}=4.41 Å, b_{COL}=2.94 Å, c=10.91 Å) (c) and (d): Relaxed 3/5 unit cell. No clustering of the Ca_2CoO_3 layer is observed. (a = 4.90 Å, b_{RSL} = 4.68 Å, b_{COL} = 2.81 Å, c = 10.88 Å) Note that the a axis is shorter for the 3/5 cell than for the 2/3 to obtain a similar volume of the unit cell for both models.

The misfit between the two moieties (COL and RSL) can lead to local stress, which in turn can induce symmetry breaking along the b direction. The periodicity of the Ca_2CoO_3 layers may thus adapt to that of the COL, forming $(Ca_2CoO_3)_n$ clusters along the b axis rather than equidistant

rock salt units. Some clustering was indeed found in experiments performed at low temperatures by Muguerra *et al.*,[15] and also in the first principles calculations of Rébola *et al.*,[19] although with different periodicities. Experiments have shown that at low temperatures the RSL forms disordered clusters of different sizes and shapes, while at $T = 400$ K a disorder-to-order transition occurs, favoring a phase with a homogeneous RSL layer.[34]

We found such clustering of the RSL along the *b* axis for the 2/3-unit cell (Fig. 6 a+b), but a homogeneous (non-clustered) RSL in the case of the 3/5 unit cell (Fig. 6 c+d). However, in all our DFT optimizations we obtained a few local minima similar in total energy, but with different symmetry of the RSL. For example, for the 3/5 model, the structure with a homogeneous RSL was found to be more stable than a clustered one by only 320 meV/cell. The determination of the precise form of the clustered phase goes beyond the scope of this study, as many quasi-equivalent energy minima are expected. Therefore we may in the following consider the 2/3 cell as a model for the clustered (low *T*) phase, and the 3/5 cell as a model for phase with a homogeneous RSL (high *T*).

In order to compute the preferred site of oxygen vacancies, we have - via Eq. 3 - calculated the formation enthalpy of a positively charged oxygen vacancy placed at different lattice sites in the structure. We considered three different positions for the oxygen vacancy: In the COL, within the outer Ca-O layer of the RSL, and in the inner Co-O layer of the RSL. For the considered 2/3 and 3/5 unit cells the stoichiometry of CCO can be written as $Ca_3Co_{3.75}O_{9-\delta}$ and $Ca_3Co_4O_{9.5-\delta}$, respectively, with $\delta = 0.25$ when one oxygen atom is removed.

The description of the localized Co(*d*) states is often improved by the inclusion of a Hubbard-like correlation (GGA+*U*).[35] However, our calculations with $U = 5$ eV, as used by Rébola *et al.* and similar to *U* values used in DFT-studies on CCO and the related compound Na_xCoO_2,[19, 36-37]

did not give reasonable results and are therefore omitted from the present paper. The formation enthalpies as obtained by DFT are reported in Table 1. The obtained values for the same defect position differ significantly for the different models, indicating the sensitivity of the electronic structure to the chosen unit cell, as discussed below. Nevertheless, common for both models considered, we found the ΔH_{form} of oxygen vacancies formed in the RSL to be lower than that of vacancies in the COL.

Table 1. Enthalpies of formation for the $v_O^{\bullet\bullet}$ defect placed in different crystallographic positions and for the different theoretical models we adopted.

	$\Delta H_{\text{form}}\ v_O^{\bullet\bullet}$ Inner-RSL (eV)	$\Delta H_{\text{form}}\ v_O^{\bullet\bullet}$ Outer-RSL (eV)	$\Delta H_{\text{form}}\ v_O^{\bullet\bullet}$ COL (eV)
2/3 cell	2.13	2.34	3.40
3/5 cell	0.41	2.90	3.23

The smallest formation enthalpy was calculated for the inner part of the RSL. This is hence the most stable site for $v_O^{\bullet\bullet}$, being somewhat more favorable ($\geq$ 200 meV) than a vacancy in the outer RSL. The defect in the COL is much less stable. We did not find any significant deviations in formation energy between vacancies placed at the different oxygen sites within the clustered rock salt layer (for the 2/3 cell).

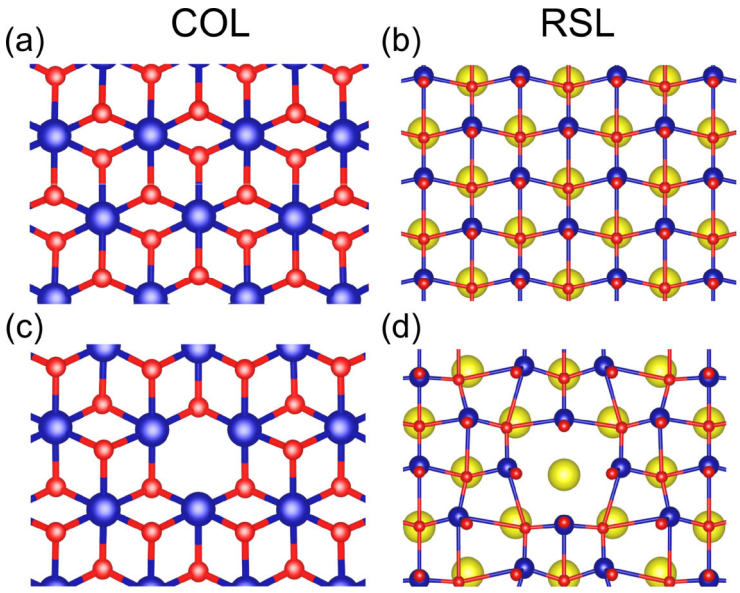

Figure 7. Geometries as obtained by DFT of the (a) pristine COL, (b) pristine RSL, (c) COL-$v_O^{\bullet\bullet}$, and (d) RSL-$v_O^{\bullet\bullet}$ seen from the (001) direction. While no structural rearrangement is seen for the vacancy inside the COL (c), lattice relaxation occurs around the vacancy in the RSL (d), effectively stabilizing the defect.

The structural changes upon oxygen vacancy formation in the COL and RSL are shown in Fig. 7 (for the 3/5 structure). For the $v_{O,RSL}^{\bullet\bullet}$-defect, we found a strong rearrangement of the co-planar Co and O ions, which move away from the defect site, while both the Ca and the O ions lying in the outer part of the RSL undergo only negligible shifts (Fig. 7 b+d). The Co-Co distances change from 4.87 to 5.10 Å along the *a*-axis, and from 4.68 to 5.49 Å along the *b*-axis. This distortion and the consequent structural stress on the RSL induce locally a clustering along the *b* axis in all the models we have studied, resulting in a structure similar to that found by Rébola *et al.* for the corresponding pristine cell.

For the $v_{O,COL}^{\bullet\bullet}$-defect, the vacancy formation induces only minimal lattice rearrangement in the CoO_2 oxide layer, where the Co ions relax about 0.1 Å toward the vacancy site (Fig. 7 a+c). We

therefore suggest that the larger relaxation around the vacancy may be one of the contributions which stabilize the vacancy defect in the RSL with respect to the COL. As these results were obtained with the 3/5-cell, we note that we qualitatively found the same results for the defects formed for the 2/3-unit cell. As the pristine structure in that case already showed clustering of the RSL, the lattice rearrangement upon formation of a $v_{O,RSL}^{\bullet\bullet}$ -defect was less effective in stabilizing the defective structure, resulting in higher formation enthalpies for the 2/3 than for the 3/5 cell.

As pointed out earlier, the 3/5 cell with a homogeneous RSL can be considered to model the high temperature phase ($T > 400$ K) of CCO, thus mimicking the experimental conditions of the TG- and TG-DSC measurements. Indeed, the oxygen vacancy formation enthalpy ΔH_{form} of 0.41 eV calculated by DFT for this cell compares favorably with the experimentally determined values (0.5-0.6 eV), suggesting that the defect formation process is appropriately described by our computational approach.

Identifying the energetically most favorable site of an oxygen vacancy to be inside the central Co-O layer of the RSL confirms the conclusion drawn from our Raman-spectroscopy results and the structural study by Ling *et al.*.[6] Furthermore, our finding of high formation energies for an oxygen vacancy placed in the COL, is in agreement with our previous calculations on Na_xCoO_2 ,[10] and indicate that the layer of edge-sharing CoO_6 octahedra – the common structural element of the misfit cobaltite family – is generally stable towards oxygen loss.

As the defect formation enthalpies in Table 1 appear to be sensitive to the chosen model, we now inspect the electronic properties of the investigated models in more detail. The electronic structures for the pristine cells computed are shown in Fig. 8. The obtained band structures are in general agreement with the calculations performed by Rébola *et al.*.[19] The states close to E_F are mostly due to hybridized Co(*d*)-O(*p*) states. The COL states are split in the octahedral crystal

field to form t_{2g} – e_g states. On the other hand - as expected for the rock salt coordination - the RSL Co(*d*)-states are not split into t_{2g} – e_g states, but appear spread over a broad energy range.

The 2/3 cell (Fig. 8 a) is half-metallic, with a 0.75 eV gap in one of the spin channels, while the 3/5-cell (Fig. 8 b) is metallic, and the gap is shifted to higher energies, from about 0.25 eV above the Fermi energy.

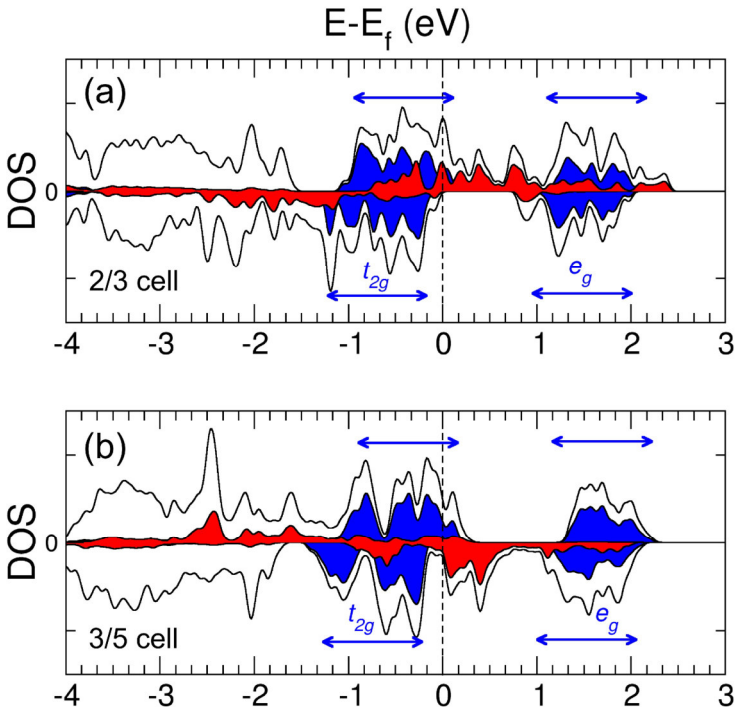

Figure 8. Density of states (DOS) plot for CCO obtained from (a) the 2/3 model and (b) the 3/5 model. The *d* states are shown filled in red (RSL) or blue (COL). The positive and negative part of the DOS corresponds to spin up and down states, respectively.

In both the 2/3 and 3/5 model, the t_{2g} orbitals are fully occupied for one of the spin components and only partially occupied for the other. This implies a mixed valence scenario for the COL, where most of the Co ions are in a +3 oxidation state with itinerant holes (representing

Co^{4+} states) contributing to the electrical conduction, as confirmed by Hall measurements.[21, 38] On the other hand, the e_g states are empty for both models.

Furthermore, we find RSL states to contribute to the total DOS at E_F for both models, contradicting experimental results of Takeuchi *et al.*,[39] which find only COL states at the top of the valence band. We ascribe the differences in Fig. 8 between the 2/3 and 3/5 cell to the different RSL symmetry in both models, in agreement with Rébola *et al.,* suggesting that the density of states close to E_F is strongly influenced by the formation of $(Ca_2CoO_3)_n$ clusters within the RSL.[19]

Each of our models fits to some of the experimental findings, but none is capable of reproducing the whole electronic structure of CCO. Therefore, we cannot conclude, which of the studied models is the most realistic approximation to describe CCO. Extending the approximate unit cell along *b* (5/8, 8/13-cells) may improve the agreement between computational and experimental results. However, such an increase in unit cell size would increase the computational effort significantly. This is in particular true for defect formation calculations, as multiples of the unit cell along the shortest lattice parameters (*a* for CCO) need to be included to avoid interactions between periodic defect images. The accumulated magnitude of these and other sources of error is difficult to quantify without efforts beyond the scope of this work. Nevertheless, the good correspondence between the calculated and measured values of the formation energy indicates that the chosen atomistic models are indeed relevant for the physical system. Moreover and most importantly, we find the relative cost of forming oxygen vacancies at various sites to be robust with respect to all tested parameters, providing computational evidence that the main loss of oxygen takes place from the central Co-O layer of the RSL.

5. Conclusion

In summary, we have studied the position and thermodynamics of oxygen vacancies in $(Ca_2CoO_3)_{0.62}(CoO_2)$ both theoretically and experimentally.

By simultaneous measurements of the weight and enthalpy change (TG-DSC), the molar oxidation enthalpy ΔH_{Ox} for temperatures between 950 and 1100 K was measured to be in the range of -39 to -68 kJ/mol (corresponding to a formation enthalpy ΔH_{form} of 0.40 - 0.71 eV per oxygen vacancy), confirming predictions made from a previously published defect chemical model (ΔH_{Ox} = -53 kJ/mol, corresponding to ΔH_{form}= 0.57 eV).

Raman spectra of a series of CCO samples prepared with different oxygen vacancy concentrations δ were taken at room temperature. We interpreted the observed depletion of a sharp mode at 700 cm^{-1} with increasing δ as an indication that oxygen vacancies are predominantly formed within the central Co-O-layer of the Ca_2CoO_3-subsystem.

This was confirmed by DFT calculations on different structural models of CCO, which found the lowest oxygen vacancy formation enthalpy ΔH_{form} for the same site. Strong defect induced lattice rearrangement of the Ca_2CoO_3 subsystem led to a computational ΔH_{form} = 0.41 eV (corresponding to ΔH_{Ox} = -40 kJ/mol) in good agreement with the experimental values. The electronic properties calculated by DFT are sensitive to the employed structural model, thereby demonstrating the difficulties of a detailed computational analysis of misfit compounds. Nevertheless, this study showed how different techniques can be used to obtain fundamental and detailed understanding of defects and their effect on functional materials in general, and the high temperature properties of $(Ca_2CoO_3)_{0.62}(CoO_2)$ in particular.

Acknowledgement

Andreas Løken is thanked for assistance recording the TG-DSC measurements. This work was funded by the Research Council of Norway via the RENERGI program (Project-No. 200022, Thermel). The DFT calculations were performed with a grant (No. nn2615k) from the supercomputing consortium NOTUR.

References

1. Hébert, S.; Kobayashi, W.; Muguerra, H.; Bréard, Y.; Raghavendra, N.; Gascoin, F.; Guilmeau, E.; Maignan, A., From Oxides to Selenides and Sulfides: The Richness of the CdI_2 type Crystallographic Structure for Thermoelectric Properties. *Phys. Status Solidi A* **2013,** *210*, 69-81.
2. Masset, A. C.; Michel, C.; Maignan, A.; Hervieu, M.; Toulemonde, O.; Studer, F.; Raveau, B.; Hejtmanek, J., Misfit-layered Cobaltite with an Anisotropic Giant Magnetoresistance: $Ca_3Co_4O_9$. *Phys. Rev. B* **2000,** *62*, 166-175.
3. Yang, G.; Ramasse, Q.; Klie, R. F., Direct Measurement of Charge Transfer in Thermoelectric $Ca_3Co_4O_9$. *Phys. Rev. B* **2008,** *78*, 153109.
4. Karppinen, M.; Fjellvåg, H.; Konno, T.; Morita, Y.; Motohashi, T.; Yamauchi, H., Evidence for Oxygen Vacancies in Misfit-Layered Calcium Cobalt Oxide, $[CoCa_2O_3]_qCoO_2$. *Chem. Mater.* **2004,** *16*, 2790-2793.
5. Lambert, S.; Leligny, H.; Grebille, D., Three Forms of the Misfit Layered Cobaltite $[Ca_2CoO_3]$ $[CoO_2]_{1.62}$ - A 4D Structural Investigation. *J. Solid State Chem.* **2001,** *160*, 322 - 331.
6. Ling, C. D.; Aivazian, K.; Schmid, S.; Jensen, P., Structural Investigation of Oxygen Non-stoichiometry and Cation Doping in Misfit-layered Thermoelectric $(Ca_2CoO_{3-x})(CoO_2)_\delta$, $\delta \approx 1.61$. *J. Solid State Chem.* **2007,** *180*, 1446 - 1455.
7. Fergus, J. W., Oxide Materials for High Temperature Thermoelectric Energy Conversion. *J. Eur. Ceram. Soc.* **2012,** *32*, 525 - 540.
8. F. Kröger, H. V., Relations between the Concentrations of Imperfections in Crystalline Solids. In *Solid state phys*, F. Seitz, D. T., Ed. Academic Press: 1956; Vol. 3, pp 307-435.
9. Tsai, P. H.; Norby, T.; Tan, T. T.; Donelson, R.; Chen, Z. D.; Li, S., Correlation of Oxygen Vacancy Concentration and Thermoelectric Properties in $Na_{0.73}CoO_{2-\delta}$. *Appl Phys Lett* **2010,** *96*, 141905.
10. Casolo, S.; Løvvik, O. M.; Fjeld, H.; Norby, T., Theoretical Analysis of Oxygen Vacancies in Layered Sodium Cobaltate, $Na_xCoO_{2-\delta}$. *J. Phys. Condens. Mat.* **2012,** *24*, 475505.
11. Vengust, D.; Jancar, B.; Sestan, A.; Ponikvar Svet, M.; Budic, B.; Suvorov, D., Chemical Decomposition as a Likely Source of Ambient and Thermal Instabilities of Layered Sodium Cobaltate. *Chem. Mater.* **2013,** *25*, 4791-4797.
12. Shu, G. J.; Lee, W. L.; Huang, F.-T.; Chu, M.-W.; Lee, P. A.; Chou, F. C., Oxygen Nonstoichiometry and the Origin of Na Ion Ordering in *P*2-Na_xCoO_2. *Phys. Rev. B* **2010,** *82*, 054106.
13. Shimoyama, J.-I.; Horii, S.; Otzschi, K.; Sano, M.; Kishio, K., Oxygen Nonstoichiometry in Layered Cobaltite $Ca_3Co_4O_y$. *Jpn. J. Appl. Phys.* **2003,** *42*, L194-L197.

14. Moser, D.; Karvonen, L.; Populoh, S.; Trottmann, M.; Weidenkaff, A., Influence of the Oxygen Content on Thermoelectric Properties of $Ca_{3-x}Bi_xCo_4O_{9+\delta}$ System. *Solid State Sci.* **2011,** *13*, 2160-2164.
15. Muguerra, H.; Grebille, D.; Bourée, F., Disordered Misfit $[Ca_2CoO_3][CoO_2]_{1.62}$ Structure Revisited via a new Intrinsic Modulation. *Acta Crystallogr. B* **2008,** *64*, 144-153.
16. Miyazaki, Y.; Onoda, M.; Oku, T.; Kikuchi, M.; Ishii, Y.; Ono, Y.; Morii, Y.; Kajitani, T., Modulated Structure of the Thermoelectric Compound $[Ca_2CoO_3]_{0.62}CoO_2$. *J. Phys. Soc. Jpn.* **2002,** *71*, 491-497.
17. Bakken, E.; Norby, T.; Stølen, S., Nonstoichiometry and Reductive Decomposition of $CaMnO_3$. *Solid State Ionics* **2005,** *176*, 217-223.
18. Mizusaki, J.; Mima, Y.; Yamauchi, S.; Fueki, K.; Tagawa, H., Nonstoichiometry of the Perovskite-type Oxides $La_{1-x}Sr_xCoO_{3-\delta}$. *J. Solid State Chem.* **1989,** *80*, 102 - 111.
19. Rébola, A.; Klie, R.; Zapol, P.; Ögüt, S., First-principles Study of the Atomic and Electronic Structures of Misfit-layered Calcium Cobaltite $(Ca_2CoO_3)(CoO_2)_{1.62}$ using Rational Approximants. *Phys. Rev. B* **2012,** *85*, 155132.
20. Asahi, R.; Sugiyama, J.; Tani, T., Electronic Structure of Misfit-layered Calcium Cobaltite. *Phys. Rev. B* **2002,** *66*, 155103.
21. Schrade, M.; Fjeld, H.; Finstad, T. G.; Norby, T., Electronic Transport Properties of $[Ca_2CoO_{3-\delta}]_q[CoO_2]$. *J. Phys. Chem. C* **2014**, 2908-2918.
22. Norby, T., Emf Method Determination of Conductivity Contributions from Protons and Other Foreign Ions in Oxides. *Solid State Ionics* **1988,** *28*, 1586-1591.
23. Kresse, G.; Hafner, J., *Ab Initio* Molecular Dynamics for Liquid Metals. *Phys. Rev. B* **1993,** *47*, 558-561.
24. Blöchl, P. E., Projector Augmented-wave Method. *Phys. Rev. B* **1994,** *50*, 17953-17979.
25. Perdew, J. P.; Burke, K.; Ernzerhof, M., Generalized Gradient Approximation Made Simple. *Phys. Rev. Lett.* **1996,** *77*, 3865-3868.
26. Van de Walle, C. G.; Martin, R. M., Theoretical Study of Band Offsets at Semiconductor Interfaces. *Phys. Rev. B* **1987,** *35*, 8154-8165.
27. Mattila, T.; Zunger, A., Deep Electronic Gap Levels Induced by Isovalent P and As Impurities in GaN. *Phys. Rev. B* **1998,** *58*, 1367-1373.
28. Zhang, S. B.; Northrup, J. E., Chemical Potential Dependence of Defect Formation Energies in GaAs: Application to Ga Self-diffusion. *Phys. Rev. Lett.* **1991,** *67*, 2339-2342.
29. Norby, T., A Kröger-Vink Compatible Notation for Defects in Inherently Defective Sublattices. *J. Korean Ceram. Soc.* **2010,** *47*, 19-25.
30. An, M.; Yuan, S. K.; Wu, Y.; Zhang, Q. M.; Luo, X. G.; Chen, X. H., Raman Spectra of a Misfit Layered $Ca_3Co_4O_9$ Single Crystal. *Phys. Rev. B* **2007,** *76*, 024305.
31. Lemmens, P.; Choi, K. Y.; Gnezdilov, V.; Sherman, E. Y.; Chen, D. P.; Lin, C. T.; Chou, F. C.; Keimer, B., Anomalous Electronic Raman Scattering in Na_xCoO_2 yH_2O. *Phys. Rev. Lett.* **2006,** *96*, 167204.
32. Tsai, P.-H.; Assadi, M. H. N.; Zhang, T.; Ulrich, C.; Tan, T. T.; Donelson, R.; Li, S., Immobilization of Na Ions for Substantial Power Factor Enhancement: Site-Specific Defect Engineering in $Na_{0.8}CoO_2$. *J. Phys. Chem. C* **2012,** *116*, 4324-4329.
33. Sudakar, C.; Kharel, P.; Lawes, G.; Suryanarayanan, R.; Naik, R.; Naik, V. M., Raman Spectroscopic Studies of Oxygen Defects in Co-doped ZnO Films exhibiting Room-temperature Ferromagnetism. *J. Phys. Condens. Mat.* **2007,** *19*, 026212.
34. Muguerra, H.; Grebille, D., Original Disorder-order Transition Related to Electronic and

Magnetic Properties in the Thermoelectric Misfit Phase $[Ca_2CoO_3][CoO_2]_{1.62}$. *Acta Crystallogr. B* **2008,** *64*, 676-683.
35. Dudarev, S. L.; Botton, G. A.; Savrasov, S. Y.; Humphreys, C. J.; Sutton, A. P., Electron-energy-loss Spectra and the Structural Stability of Nickel Oxide:An LSDA+U Study. *Phys. Rev. B* **1998,** *57*, 1505-1509.
36. Singh, D. J., Electronic Structure of $NaCo_2O_4$. *Phys. Rev. B* **2000,** *61*, 13397-13402.
37. Zhang, P.; Luo, W.; Crespi, V. H.; Cohen, M. L.; Louie, S. G., Doping Effects on the Electronic and Structural Properties of CoO_2: An LSDA+*U* Study. *Phys. Rev. B* **2004,** *70*, 085108.
38. Eng, H. W.; Limelette, P.; Prellier, W.; Simon, C.; Frésard, R., Unconventional Hall effect in Oriented $Ca_3Co_4O_9$ Thin Films. *Phys. Rev. B* **2006,** *73*, 033403.
39. Takeuchi, T.; Kondo, T.; Takami, T.; Takahashi, H.; Ikuta, H.; Mizutani, U.; Soda, K.; Funahashi, R.; Shikano, M.; Mikami, M., et al., Contribution of Electronic Structure to the Large Thermoelectric Power in Layered Cobalt Oxides. *Phys. Rev. B* **2004,** *69*, 125410.

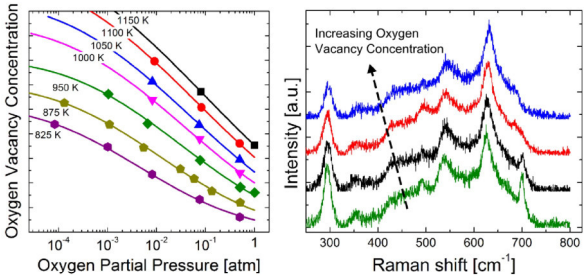
Oxygen Vacancy Concentration
1150 K
1100 K
1050 K
1000 K
950 K
875 K
825 K
10^{-4}
10^{-3}
10^{-2}
10^{-1}
1
Oxygen Partial Pressure [atm]
Intensity [a.u.]
Increasing Oxygen
Vacancy Concentration
300
400
500
600
700
800
Raman shift [cm^{-1}]